

# Studies of an air-shower imaging system for the detection of ultrahigh-energy neutrinos

Adam Nepomuk Otte\*

*School of Physics & Center for Relativistic Astrophysics,  
Georgia Institute of Technology 837 State Street NW, Atlanta, Georgia 30332-0430, USA \**

(Dated: February 15, 2022)

We discuss the acceptance and sensitivity of a small air-shower imaging system to detect earth-skimming ultrahigh-energy tau neutrinos. The instrument we study is located on top of a mountain and has an azimuthal field of view of  $360^\circ$ . We find that the acceptance and sensitivity of such a system is close to maximal if it is located about 2 km above ground, has a vertical field of view of  $5^\circ$ , allows the reconstruction of an at least  $0.3^\circ$  long air-shower image, and features an effective light-collection area of  $10 \text{ m}^2$  in any direction. After three years of operation, an imaging system with these features achieves an all-flavor neutrino flux sensitivity of  $5 \times 10^{-9} \text{ GeV cm}^{-2} \text{ s}^{-1} \text{ sr}^{-1}$  at  $2 \times 10^8 \text{ GeV}$ .

## I. INTRODUCTION

The window to high-energy (HE) neutrino astronomy was recently opened by the IceCube Collaboration with the detection of an astrophysical neutrino flux [1], and evidence that supports the idea of blazars being a source of neutrinos [2, 3]. The latter conclusion comes from a correlation between the arrival time of IceCube detected neutrinos and the observation of a flare in the electromagnetic band, which highlights the importance of the multimessenger approach in modern astrophysics. The detection of HE neutrinos raises a number of interesting questions that are potentially answered by neutrino observations at higher energies: What are the astrophysical sources of these neutrinos (see [4–7] and references in [8])? Are blazars really a source of neutrinos? What other sources of HE neutrinos are there? These questions can be addressed by extending the spectral measurements of the astrophysical neutrino flux to higher energies and by reconstructing the arrival direction of neutrinos with better angular resolution.

But, hunting down astrophysical neutrinos is not the only science case for ultrahigh-energy (UHE,  $> 1 \text{ PeV}$ ) neutrino detectors; the long-standing quest to understand the composition and the sources of UHE cosmic rays is another one. The connection between neutrinos and cosmic rays is made when UHE cosmic rays interact with cosmic microwave background photons. The number of neutrinos produced in these interactions depends on the composition of the cosmic rays [9]. While recent measurements with cosmic-ray experiments favor a heavier composition [10–15], UHE neutrino observations would not only independently confirm these findings but, more importantly, provide a unique handle to constrain source models of UHE cosmic rays [16]. Furthermore, would a combination of UHE neutrino measurements with proton measurements obtained with next-generation UHE cosmic-ray observatories (e.g. Auger-

Prime) allow one to simultaneously constrain the UHE proton fraction and source evolution [17].

A third science case is tests of neutrino physics at the highest energies, which could potentially hint at new physics beyond the standard model [18–22]. One approach would be to compare neutrino fluxes measured with experiments that are sensitive to different neutrino flavors. In that context it is noteworthy that experiments geared toward measuring extraterrestrial neutrinos have already provided numerous important contributions to neutrino physics [23–28]. Adding to the discovery potential for new physics is the detection of neutrino candidates with ANITA, which have signatures expected from air showers but seem to contradict the current understanding of neutrino physics [19, 29].

While the existence of  $10^9 \text{ GeV}$  neutrinos is noncontroversial and efforts to hunt them are admirable, actually detecting them is a daunting task. The two biggest challenges are the minute neutrino cross section and the extremely low UHE neutrino flux. Both are overcome by instrumenting large detection volumes in a cost-effective way.

At present, the efforts to detect UHE neutrinos can be divided into two approaches. The first approach is to utilize, like IceCube or ANTARES/KM3Net [30, 31], large volumes of ice or water, in which a neutrino interacts and a particle shower develops. In fact, IceCube itself has sensitivity to UHE neutrinos and the published IceCube limits are the presently most constraining ones up to about  $10^{11} \text{ GeV}$  [32]. The ARA [33, 34], ARIANNA [35, 36], and ANITA Collaborations [37–39] also use ice as a detection medium and either deploy radio antennas in ice (ARA, ARIANNA) or look for a particle shower induced radio signature from a balloon (ANITA). For reviews about the detection of air showers with radio and a more complete list of experiments that use or plan to use radio for the detection of UHE neutrinos see [40, 41].

The second approach is the so-called earth-skimming technique. In the earth-skimming technique, a UHE tau neutrino interacts within tens to hundreds of kilometers inside Earth after entering it. The tau produced in the interaction continues to propagate through Earth and

---

\* otte@gatech.edu

emerges from the ground if it does not decay before. If it emerges, the tau decays in the atmosphere and initiates an air shower, which is then detected [42–47].

All major air-shower detecting astroparticle experiments also search for tau neutrinos, even though these instruments are designed to detect gamma rays or ultrahigh-energy cosmic rays and are not optimized for tau-neutrino detection. For example, the Pierre Auger Collaboration has published competitive limits above  $10^8$  GeV [48–50].

The most recent limit from a gamma-ray Cherenkov telescope comes from the MAGIC Collaboration. They report a limit on the diffuse neutrino flux, which was obtained by pointing the MAGIC telescopes at the sea during times when gamma-ray observations could not take place due to clouds [51, 52].

Because these experiments are not optimized for earth-skimming neutrino detections and in the case of pointed instruments like MAGIC have only a little time to spare for neutrino searches, it is not surprising that several efforts are ongoing to design and build dedicated earth-skimming neutrino detectors. One such project is GRAND [18, 53, 54], which aims at the detection of radio emission from tau initiated air showers by distributing several thousand antennas over an about 100 000 km<sup>2</sup> large area in the Himalayas.

Another proposed experiment is NTA, which evolved from Ashra and uses the air-shower imaging technique [55, 56]. For NTA, four optical detector stations are proposed at Mauna Loa, Hawaii, of which three are located on opposite mountains and the fourth one in between them. One NTA detector station consists of several units. One unit is composed of four independent 1.5 m diameter mirrors each with one camera. The resolution of one camera is  $0.125^\circ$  [55]. Prototype detector stations have been built and operated [57].

The CHANT proposal discusses the deployment of a Cherenkov telescope system on a long duration balloon flight or a satellite [58]. The idea is now pursued as part of SPB2 [59] and POEMMA [60]. Other experiments proposed in the past to image air showers induced by taus are reported in [61–63].

In this paper we discuss the acceptance and sensitivity of an air-shower imaging detector, which is located on top of a mountain, which has an unobstructed  $360^\circ$  azimuthal field of view, and which uses the earth-skimming technique. Our motivation is to understand (a) the sensitivity of such an instrument to UHE neutrinos, (b) the impact of different detector parameters on the sensitivity, and (c) the minimal detector configuration, which results in a close to optimal sensitivity.

The main objective of the instrument would be to establish a diffuse UHE neutrino flux. We thus do not go into a discussion of optimizing the reconstruction of the energy and arrival direction of tau neutrinos. The imaging technique, however, can provide energy resolution better than 20% and angular resolution better than  $0.2^\circ$ ; see e.g. [64].

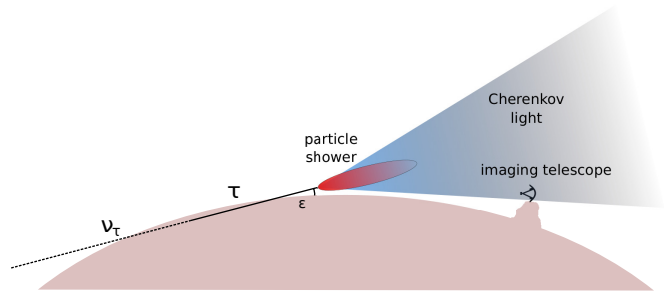


FIG. 1. Not-to-scale sketch of the earth-skimming technique and the emission cone of Cherenkov light produced by charged shower particles. An imaging system, receptive to Cherenkov and fluorescence light, is located on a mountain and takes an image of the air shower by collecting some of the light.

We start the paper by introducing the experimental setup, i.e. the topography assumed in the earth-skimming technique and the detector layout. We then continue with the calculation of the joint probability that a tau neutrino interacts inside Earth and a tau emerges from the ground. The calculation is followed by a discussion of the consequences for the design of an air-shower imaging experiment, which arise from the geometry of the air shower that develops in the atmosphere. The implications of the air-shower geometry and the emission pattern of the light from the air shower on the light intensity at the detector are discussed in the subsequent section followed by a discussion of the acceptance and the sensitivity for different detector configurations. Before closing with concluding remarks, we briefly present design considerations for an actual instrument we dub *Trinity*.

## II. EARTH-SKIMMING TECHNIQUE

Figure 1 shows the principle of the earth-skimming technique. A tau neutrino enters Earth, interacts and produces a tau. The tau propagates through Earth and, if it has not yet decayed, emerges from the ground with an angle  $\epsilon$ , which is the same angle under which the neutrino has entered Earth. For this study we approximate Earth as a smooth sphere, i.e. without structure and with a radius of 6371 km.

If the tau decays in the atmosphere, a muon is produced in 17% of the cases, which traverses the atmosphere without further interaction and cannot be detected. Another 17% of the decays produce electrons, which initiate electromagnetic showers. The remaining 66% of the decays result in charged and neutral pions, which further decay into muons and gammas. The gammas initiate electromagnetic showers, whereas the majority of muons leave the atmosphere without further interaction. The charged shower particles radiate about 0.1% of the shower energy as Cherenkov radiation, which is beamed forward in a cone around the shower axis. The

photon intensity is approximately constant within the cone out to an angle of about  $1^\circ$  from the shower axis and drops exponentially for larger angles. We show later that the emission is intense enough to be detected, even if the shower is several hundred kilometers away. If the shower develops within tens of kilometers from the detector, the shower can be imaged from all angles with the fluorescence light that is emitted from nitrogen molecules in the atmosphere, which are excited by collisions with shower particles.

The earth-skimming technique is only suitable for the detection of tau neutrinos, even though the interaction cross section is about the same for all neutrino flavors in the UHE band [65] and equal interaction rates are therefore expected for all flavors. But electron neutrinos generate electrons, which immediately produce a particle shower inside Earth. Muons produced in muon neutrino interactions, on the other hand, emerge from the ground but the probability for them to decay or interact within the field of view of a ground based instrument and produce an air shower is negligible. While the muon itself emits Cherenkov light, the intensity is so low that it would only be detectable if the muon comes within a few hundred meters of the detector, which is unlikely. Only taus decay and produce an air shower within the field of view of a suitable instrument with sufficiently high probability.

The imaging of air showers is a very successful technique used by a number of very high-energy gamma-ray instruments [66–69] and ultrahigh-energy cosmic-ray experiments [70, 71]. Sensitivity determining factors of an imaging system are the following:

- i) The probability that a tau neutrino interacts on its path through Earth and a tau emerges from the ground.
- ii) The probability that the tau decays and a particle shower develops within the field of view of the instrument.
- iii) The intensity of the Cherenkov/fluorescence light emitted in the direction of the instrument is above the detection threshold of the instrument.
- iv) The ability to reconstruct the event with the recorded image and reject the event if it is not a tau neutrino.

The first three points determine the detector acceptance at trigger level

$$\Phi(E_\nu) = \int_A \int_\Omega \int_{E_\tau} P_{\text{det}}(E_\tau) \cdot P(E_\tau|E_\nu, \epsilon) \cdot \sin(\epsilon) dE_\tau dA d\Omega \quad (1)$$

where  $P$  is the joint probability that a neutrino with energy  $E_\nu$  interacts, a tau emerges from the ground, and a particle shower is initiated.  $P$  depends on the elevation

angle  $\epsilon$  of the emerging tau and its energy  $E_\tau$ . We discuss in the next section how we calculate  $P$ .  $P_{\text{det}}$  is the probability that an air shower initiated by a tau with energy  $E_\tau$  is detected. It depends on the distance between the air shower and the detector,  $\epsilon$ , the angle of the shower axis to the detector  $\alpha$  (see later), and the detector configuration. The acceptance is integrated over the plane  $A$  defined by the telescope location and the horizon in a given direction. The elevation  $\epsilon$  is measured relative to that plane.

We point out that the sensitivity of an earth-skimming experiment is mostly determined by the topography of the area surrounding the detector. Throughout the paper, we approximate Earth as a smooth sphere, and the imaging system is assumed to be located on a mountain, which provides an unobstructed  $360^\circ$  azimuthal field of view. We do not claim that this is the best possible configuration. On the contrary, we view our choice as a baseline configuration and are open to the idea that other topographies result in better sensitivities.

### III. PROBABILITY OF NEUTRINO INTERACTION AND TAU EMERGENCE

We calculate the probability of a neutrino interacting and a tau emerging from the ground with the parametrization from [72], which includes a treatment of the tau energy losses. But the parametrization does not include neutrino regeneration effects [73, 74], and our calculations thus underestimate the detectability of tau neutrinos below  $10^8$  GeV.

We use Eq. (28) of [72] to calculate the interaction probability of a tau neutrino with energy  $E_\nu$  and the emergence probability of a tau with energy  $E_\tau$  as

$$P = \frac{1}{\beta \rho E_\tau} \cdot P_\nu \cdot P_\tau \quad (2)$$

where the neutrino interaction probability is

$$P_\nu = \sigma_{CC} \rho N_A \exp[-D_\nu(\sigma_{CC} + \sigma_{NC})\rho N_A] \quad (3)$$

and the probability for the tau to emerge from the ground is

$$P_\tau = \exp[-m_\tau/(\tau_\tau c \beta \rho E_\tau) \cdot (1 - e^{-\beta \rho D_\tau})], \quad (4)$$

where  $\rho = 2.65 \text{ g/cm}^3$  is the density of rock and  $\sigma_{CC}$  and  $\sigma_{NC}$  are the energy dependent charged and neutral current neutrino cross sections from [65].  $N_A$  is the Avogadro constant,  $\tau_\tau$  is the lifetime of the tau,  $m_\tau$  is its mass, and  $c$  is the speed of light.  $D_\tau$  is the distance the tau has to travel through Earth before it emerges if its initial energy is  $0.8E_\nu$  and the energy when it emerges from the ground is supposed to be  $E_\tau$ ,

$$D_\tau = \ln[0.8E_\nu/E_\tau]/(\beta \rho). \quad (5)$$

The distance  $D_\nu$ , which is the distance the neutrino travels through the Earth before it interacts, is calculated

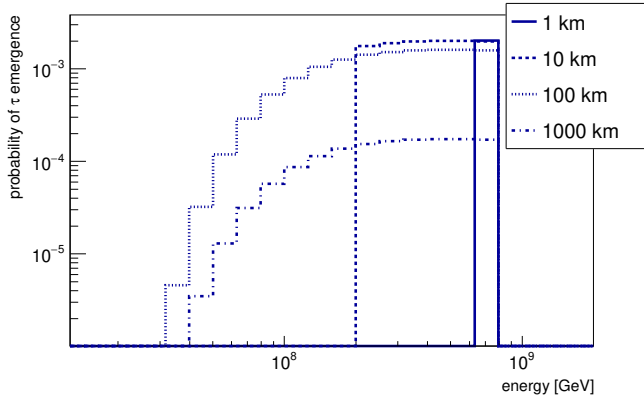


FIG. 2. Energy distribution of taus produced by  $10^9$  GeV tau neutrinos. Distributions for targets with four different thicknesses are shown. The vertical axis gives the probability that the neutrino interacts and a tau emerges from the target.

from the combined trajectory  $D$  of the tau and the neutrino through Earth,

$$D = D_\nu + D_\tau \rightarrow D_\nu = D - D_\tau. \quad (6)$$

For the energy loss  $\beta$  of the tau while it propagates through Earth we use Eq. (13) case III from [72]

$$\beta = \beta_0 + \beta_1 \ln(E/E_0) \quad (7)$$

with  $\beta_0 = 1.2 \times 10^{-6} \text{ cm}^2/\text{g}$ ,  $\beta_1 = 0.16 \times 10^{-6} \text{ cm}^2/\text{g}$ , and  $E_0 = 10^{10} \text{ GeV}$ .

As an example, we use the above parametrization to calculate the energy distribution of taus that are produced by  $10^9$  GeV neutrinos and emerge from the ground. We assume four targets with thicknesses: 1 km, 10 km, 100 km, and 1,000 km (see Fig. 2). The energy dispersion is negligible for a 1 km thick target and steadily increases for thicker targets. For a 100 km target, the dispersion covers one decade of energy.

Integrating each of the distributions gives the probability that a  $10^9$  GeV neutrino interacts and a tau emerges. This so-called emergence probability is shown in Fig. 3 for different neutrino energies as a function of target thickness. For  $10^9$  GeV neutrinos the probability steadily increases with target thickness and rapidly drops beyond 1,000 km. The axis on top of the figure shows the elevation angle  $\epsilon$  for which a neutrino entering Earth would traverse the same distance as shown on the bottom axis before reemerging from the ground [75].

For  $> 10^9$  GeV neutrinos, the emergence probability is maximal if the target is between 10 km and 500 km thick, which corresponds to elevation angles between  $0.5^\circ$  and  $2^\circ$ . For thicker targets, the taus decay inside the target and for thinner targets, the interaction probability goes down. For lower neutrino energies an optimal target thickness is less evident because of the smaller neutrino interaction cross section and the shorter tau lifetime.

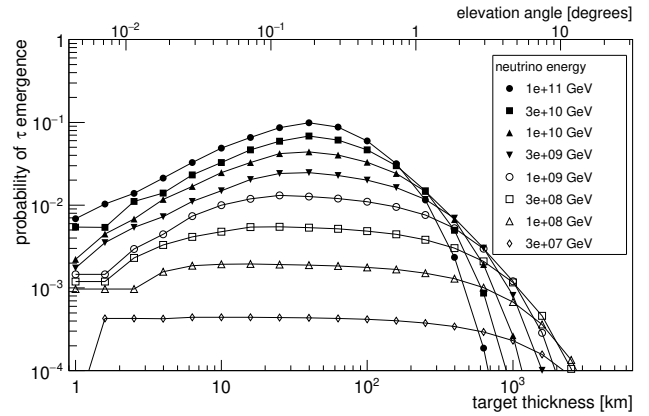


FIG. 3. Probability of a tau neutrino interacting and a tau emerging from a target with density  $\rho = 2.65 \text{ g/cm}^3$  (rock). The top axis shows the elevation angle under which a neutrino has to enter Earth in order to traverse the distance given on the bottom axis.

#### IV. GEOMETRICAL CONSTRAINTS IN AIR-SHOWER IMAGING

When a tau emerges from the ground, it decays and can induce a particle shower. The particles of the shower produce Cherenkov and fluorescence light, which is used to image the shower with an air-shower imaging instrument.

The Cherenkov and fluorescence light have very different characteristics. Cherenkov emission is beamed into the direction of shower development, whereas fluorescence emission is isotropic. Integrated over all emission angles, the Cherenkov emission is orders of magnitude more intense than the fluorescence emission. The Cherenkov spectrum is proportional to  $1/\lambda^2$  at the point of production, whereas the fluorescence light is emitted in a few narrow lines around 340 nm [76, 77]. The shape of the Cherenkov spectrum is different at the detector due to scattering and absorption in the atmosphere. We show simulated spectra later. Another striking difference is the arrival-time distribution of the photons. The Cherenkov photons arrive within a few nanoseconds if the shower is viewed head on and within several microseconds if the shower is viewed under an angle of  $30^\circ$ . We give an example of a simulated time distribution later. The fluorescence photons arrive over several microseconds. As a result of these different characteristics, showers that develop more than  $\sim 50$  km from the telescope can only be imaged with Cherenkov light. The fluorescence light becomes the dominant detection channel at closer distances.

Even though both emission mechanisms have vastly different characteristics, the requirements to record a shower image derive mostly from geometry and equally apply to both detection channels:

- The shower image has to be fully contained in the field of view of the telescope.

- Light from both ends of the air shower need to arrive at the telescope with sufficient intensity.
- The image has to be of a minimal length in order to be reconstructable.

Figure 4 shows how these requirements translate into geometrical constraints. The particle shower is depicted in the figure in relation to the imaging system with all relevant distances and angles. The trajectory of the tau and the main shower axis are represented by the arrow.

If the tau emerges below the horizon from the ground, as it is shown in Fig. 4, it first propagates a distance  $d'$  before it enters the field of view of the telescope. The distance to the telescope when the tau enters the field of view is  $l$ . The fraction of taus that has not decayed while propagating through  $d'$  is  $\exp(-d'/\lambda)$ , where the decay length is  $\lambda = E_\tau \cdot c \cdot \tau_\tau / m_\tau = 49 \text{ km} \cdot E_\tau / 10^9 \text{ GeV}$ . The decay length  $\lambda$  solely depends on the tau energy  $E_\tau$ , which is between 10% and 100% of the neutrino energy (see Fig. 2). For the neutrino energies of interest,  $10^8 \text{ GeV}$  to  $10^{10} \text{ GeV}$ , the tau energies are between  $10^7 \text{ GeV}$  and  $10^{10} \text{ GeV}$ . The distance  $d_{90} = -\ln(0.1) \cdot \lambda$  over which 90% of the taus decay is then between 1 km ( $10^7 \text{ GeV}$ ) and 1,000 km ( $10^{10} \text{ GeV}$ ).

After propagating an additional distance  $d$  in the telescope field of view, the tau decays and a particle shower is initiated, which develops over the distance  $s$ . The necessity of imaging the entire shower requires that the angle  $\phi$  has to be smaller than the field of view of the camera above the horizon and in turn sets the maximum possible value for  $d$ . If more than 90% of the taus decay over  $d$ , we readjust  $d$  to  $d_{90}$ . This is to simplify the acceptance calculation for which we would otherwise have to integrate along  $d$  and evaluate at each step in the integral if enough light reaches the detector. Instead, we assume that all taus decay when reaching the end of  $d$  and evaluate only for that situation if enough light reaches the detector from the tip of the shower, i.e. if the intensity emitted under angle  $\zeta$  is above the detection threshold of the telescope. If the intensity is below the detection threshold, we reduce  $d$  and thus  $\zeta$  until the intensity is above threshold. We do this because the Cherenkov intensity increases exponentially for smaller angles of  $\zeta$  (see later). If no value for  $d > 0$  can be found that satisfies all requirements, the shower is considered unobservable.

The length of the shower  $s$  is estimated with the Heitler model for electromagnetic showers [78, 79], which states that the number of particles doubles and the energy per particle halves for every radiation length  $X_0$  due to pair creation of gammas and bremsstrahlung by electrons/positrons. The number of particles reaches its maximum when the average energy per particle reaches the critical energy  $E_c = 88 \text{ MeV}$  for electrons in air [80]. In this model, the shower develops over

$$X = \frac{\ln(E/E_c)}{\ln(2)} \quad (8)$$

radiation lengths.

For the estimate of the shower length, we assume that 50% of the tau energy is deposited in the electromagnetic part of the shower. For the tau energies of interest (see above), the particle shower then develops over 27–37 radiation lengths. If the shower develops close to the ground, which implies that the air density is constant and one radiation length is 304 m, the shower length  $s$  is 8 km–11 km.

A constant air density is a good approximation for the development of showers initiated by  $10^7 \text{ GeV}$  taus. Even for an extreme tau emergence angle of  $10^\circ$  (see Fig. 3), the shower is fully developed at an altitude of 1.6 km. At that altitude the air density is still 80% of the density at sea level. For the highest-energy taus, the emergence probability (see Fig. 3) reaches 10% of the peak probability when the emergence angle is about  $3^\circ$ . For that angle the shower is fully developed at an altitude of 600 m above ground.

But because the decay length is much longer for high-energy taus, the shower develops higher up in the atmosphere and, therefore, over a longer distance because of the lower air density. We nevertheless use the shorter shower length calculated for an air density close to ground, which is conservative because it results in an increased number of events that are rejected because they fail the minimal-length requirement of the image in the reconstruction.

Summarizing, the detection probability of a tau,  $P_{\text{det}}$  in Eq. (1), is evaluated by calculating the probability that the tau decays inside the field of view of the camera under the constraint that the shower has to be fully contained inside the camera field of view. A shower image is considered reconstructable if its image length is above the required minimum and the detected light intensity from both ends of the shower is above the detection threshold of the telescope. The decay length  $d$  is adjusted to meet the minimum intensity requirement or, if it is shorter, the distance over which 90% of the taus decay.

## V. CHERENKOV LIGHT DENSITY

Crucial for a valid calculation of the detection probability of a tau  $P_{\text{det}}$  is a good understanding of the amount of Cherenkov light and fluorescence light reaching the detector. In this section, we discuss the Cherenkov light density followed by the fluorescence light density in the next section.

The amount of Cherenkov light, that reaches the telescope depends on the tau elevation  $\epsilon$ , azimuth  $\alpha$ , distance to the shower  $l$ , and location of the telescope above ground  $h$  as defined in Fig. 4. We derive parametrizations of the Cherenkov light intensity at the detector for four different telescope locations above ground (0 km, 1 km, 2 km, and 3 km). For the parametrization we have simulated air showers initiated by  $3 \times 10^4 \text{ GeV}$  gamma rays. We use gamma rays because they initiate pure electromagnetic showers and deposit all the energy into the

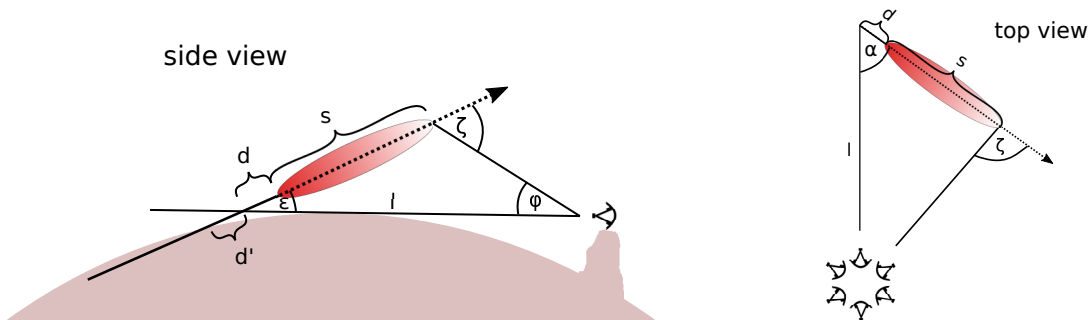


FIG. 4. Side and top views of the air shower and the imaging system to illustrate geometrical requirements, which have to be fulfilled to obtain a complete image of the shower. Two of the conditions are (a) Cherenkov light from the tip of the shower has to reach the telescope in sufficient intensity, which is constrained by the maximum Cherenkov angle  $\zeta_{\max}$ . (b) The shower needs to be fully contained in the vertical field of view  $\phi$  of the telescope. The remaining conditions are discussed in the text. The angles and distances marked in the figures are projections of their actual quantities with the exception of  $\alpha$ , which is the angle between  $l$  and the projection of the shower axis onto the ground.  $l$  is the distance between the telescope and the point where the tau enters the field of view.

shower, which for our purpose yields a robust Cherenkov light intensity per tau energy deposited in the shower (we assume that 50% of the tau energy is deposited in an electromagnetic shower). It is, furthermore, sufficient to simulate one energy because the Cherenkov intensity is proportional to the shower energy and can thus easily be scaled in the calculation of the detection probability to match the energy deposited in the shower. As a cross-check, we also derived a parametrization by simulating  $10^6$  GeV gamma rays and found both parametrizations to be in agreement.

The air showers are simulated with CORSIKA version 75000 [81], which we modified to allow the simulation of Cherenkov photons up to 900 nm. CORSIKA does not simulate Cherenkov emission for upward going showers, which is why we have configured CORSIKA with an atmosphere of constant density and have simulated straight downward going showers. The gamma rays are released at heights of 25 km, 55 km, 85 km, 135 km, and 195 km. The arrival time, wavelength, impact angle, and position of all Cherenkov photons, that reach the ground are saved.

Atmospheric absorption of the Cherenkov photons is not simulated in CORSIKA but subsequently applied. For the altitude and wavelength dependent extinction coefficients in the atmosphere, we take the model that is used by the VERITAS Collaboration in the analysis of winter season data. The model was simulated with MODTRAN [82]. Mie scattering is considered to be an absorption and not a scattering process in the model, which results in an underestimation of the Cherenkov intensity outside of the primary Cherenkov cone ( $> 1^\circ$ ) by a few percent [58, 83, 84]. Refraction in the lower atmosphere, which results in a bending of the photon trajectory along the Earth's surface and an increase in photon intensity at the telescope, is also not taken into account.

The absorption is calculated by translating and rotating the CORSIKA simulated shower such that (a) the

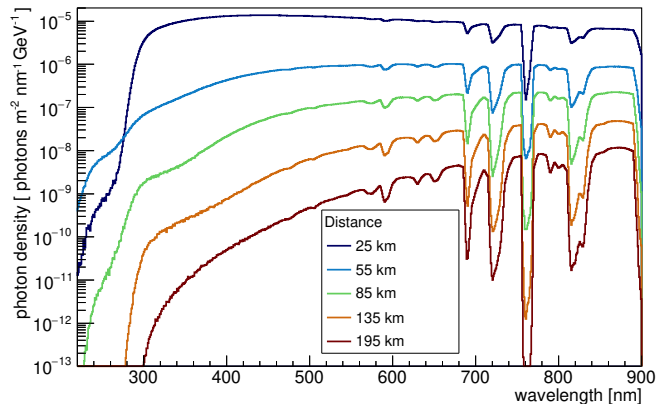


FIG. 5. Cherenkov photon spectra at the detector for showers starting in distances of 25 km, 55 km, 85 km, 135 km, and 195 km from the detector.

shower axis points upward with an elevation angle  $\epsilon$  (see Fig. 4 [85]), (b)  $d = 5$  km, and (c) the plane in which all the photons are recorded in CORSIKA intersects with the location of the telescope. Each photon in the plane is then rotated around the shower axis and the telescope is moved parallel to the ground such that the positions of the photon and the telescope coincide. The photon is then ray traced back to its origin and the absorption applied in steps of 1 km.

After absorption is applied, simulated Cherenkov spectra at the location of the telescope such as the ones in Fig. 5 are obtained. In this particular case the telescope is located 1 km above the ground, the elevation  $\epsilon$  is  $1^\circ$ , and  $\alpha$  is  $0.25^\circ$ . It is evident how the peak of the detected spectrum shifts toward longer wavelengths with an increasing distance between the telescope and the shower, from 400 nm at 25 km to 900 nm at 195 km.

The spectral response of silicon photomultipliers (SiPMs) is a good match to the heavily absorbed



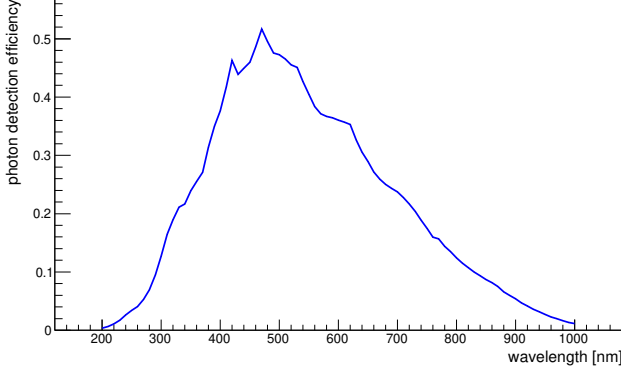


FIG. 6. Photon detection efficiency of the S14520-6050CN SiPM from Hamamatsu for a bias, which yields a 90% breakdown probability at 400 nm.

Cherenkov spectra. Reviews of SiPMs can be found in [86, 87]. For this study, we adopt the photon detection efficiency (PDE) of the Hamamatsu SiPM S14520-6050CN when it is operated at a bias voltage that yields a 90% breakdown probability at 400 nm (see Fig. 6). The PDE measurement was done with the setup described in [88]. The PDE peaks at 470 nm with 51%, the full width at half maximum of the spectral response spans from 360 nm to 680 nm, and a long tail of the PDE extends to 1000 nm. With this spectral response about 30% of the Cherenkov photons that arrive at the telescope are detected. Other characteristics of the S14520-6050CN are an optical cross talk of less than 1.5% and 50  $\mu\text{m}$  size cells [89].

Integrating the product of the simulated Cherenkov photon density and the PDE and dividing the integral by the simulated gamma-ray energy, we obtain the density of the detected Cherenkov photons (photoelectrons or pe) per GeV shower energy. Figure 7 shows the photoelectron density per GeV air-shower energy as a function of  $\alpha$  for an air shower with an elevation of  $0^\circ$  and a starting point 55 km away from the telescope. The telescope is located on the ground  $h = 0$  km. The density is roughly constant out to  $1^\circ$ , which is not evident from the coarse binning of  $0.5^\circ$  but expected [90]. Above  $1.3^\circ$ , the intensity is well described with two exponential functions

$$\rho(\alpha') = 3.32 \cdot 10^{-4} e^{-\frac{\alpha'}{0.581^\circ}} \frac{\text{pe}}{\text{m}^2 \text{GeV}} + 4.26 \cdot 10^{-5} e^{-\frac{\alpha'}{1.95^\circ + 0.0427\alpha'}} \frac{\text{pe}}{\text{m}^2 \text{GeV}}. \quad (9)$$

Note that  $\alpha'$  is the angle between the shower axis and  $l$ . In this particular case ( $\epsilon = 0^\circ$  and  $h = 0$  km),  $\alpha'$  coincides with  $\alpha$ , which is defined as the projection of  $\alpha'$  onto the plane defined in Fig. 4.

The remaining density distributions for distances of 25 km, 55 km, 85 km, 135 km, and 195 km and elevations from  $0^\circ$  to  $10^\circ$  are well described by functions of the form

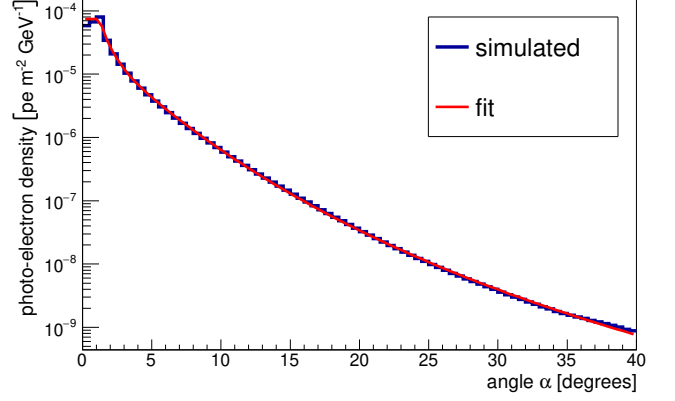


FIG. 7. Simulated (blue line) and parameterized (red line) photoelectron densities per GeV shower energy as a function of angle  $\alpha$ . The distance to the shower is 55 km, the shower elevation angle is  $0^\circ$ , and the telescope is located on the ground ( $h = 0$  km).

$$N_0 \cdot \rho(\alpha') \left( 2 - e^{-\frac{\epsilon}{\lambda_0}} \right) \cdot e^{-\frac{l-55 \text{ km}}{\lambda_1 + (l-55 \text{ km}) \cdot \lambda_2}}, \quad (10)$$

where we use  $\rho(\alpha')$  from the previous equation. Angle  $\alpha'$  is again the angle between the shower axis and  $l$  and is calculated as  $\alpha' = \sqrt{\alpha^2 + (\epsilon - \tan^{-1}(h/l))^2}$ . The best fit parameters of the photoelectron density function are listed in Table I for four different telescope heights  $h$ .

Figure 8 shows, as an example, simulated and parameterized photoelectron density distributions for a telescope located 1 km above ground and a shower elevation of  $1^\circ$ . Discrepancies between the parameterized and simulated densities are evident at small angles  $\alpha$ , while the agreement is good for large angles. Even though the discrepancy is as large as a factor of 2 at some angles, the impact on the acceptance calculation is tolerable.

The discrepancies are tolerable because the density distributions are only used to determine the integration limits for  $\alpha$  in the acceptance calculation, i.e. at what value of  $\alpha$  the photoelectron density drops below the detection threshold of the telescope. The limits for  $\alpha$  derived from the parametrization deviate by no more than  $0.5^\circ$  from the simulated value if the distance to the shower is more than 25 km. Such a small discrepancy does not have a significant impact on the acceptance calculations. At a distance of 25 km, the parametrization deviates from the simulated value by as much as  $1.5^\circ$ . This is again acceptable because the threshold for the minimal photoelectron density is reached at much larger  $\alpha$ , where the difference between simulation and parametrization is again acceptable. Furthermore, Cherenkov detected events do not contribute much to the acceptance if they originate within a few tens of kilometers from the telescope, which we show later.

Besides showing that the parametrization is a good fit to the simulated distribution, Fig. 8 also demonstrates

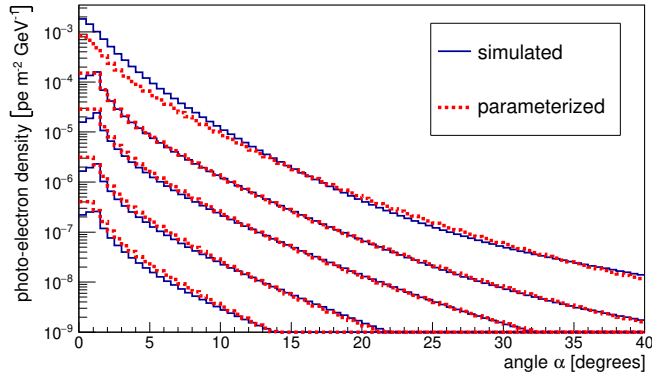


FIG. 8. Simulated (blue line) and parameterized (red line) photoelectron density distributions for a  $1^\circ$  shower elevation and a telescope location above ground of 1 km. The topmost distribution is for a 25 km distance to the shower. The distributions shown below it correspond — from top to bottom — to distances of 55 km, 85 km, 135 km, and 195 km.

that air showers can be detected out to large angles of  $\alpha$ . For example, according to the figure, a shower with  $10^8$  GeV can be detected from a distance of 195 km out to an angle  $\alpha = 5^\circ$  with a  $10\text{ m}^2$  telescope and a 24 photoelectron threshold. If the shower is 135 km away, the angle increases to  $20^\circ$ .

TABLE I. Best fit parameters for Eq. (10) for four different telescope heights above the ground.

Height (km)	$N_0$ (.)	$\lambda_0$ (degrees $10^{-4}$ )	$\lambda_1$ (km)	$\lambda_2$ ( $10^{-2}$ )
0	1	1.64	16.7	5.09
1	1.03	1.91	16.6	5.23
2	1.53	7.12	18.0	5.95
3	2.37	51.3	19.0	6.42

#### A. Arrival-time distribution of Cherenkov photons

The time during which the Cherenkov photons arrive at the detector depends on the angle  $\alpha$  and is shown in Fig. 9 for 30 TeV electromagnetic showers starting at 130 km from the telescope with an elevation angle of  $0.3^\circ$ . That elevation and distance is typical for tau-neutrino events, which contribute to the peak in the radial acceptance (see later sections). The telescope is located 2 km above the ground. Each point in the figure shows the time period centered at the median photon arrival time during which a certain fraction of Cherenkov photons arrives at the telescope if the shower is viewed under an angle  $\alpha$ . The fractions are 25%, 50%, 75%, and 90%.

If  $\alpha$  is less than  $3^\circ$ , 50% of the Cherenkov photons arrive at the detector within 10 ns. If  $\alpha$  is  $10^\circ$ , 50% of

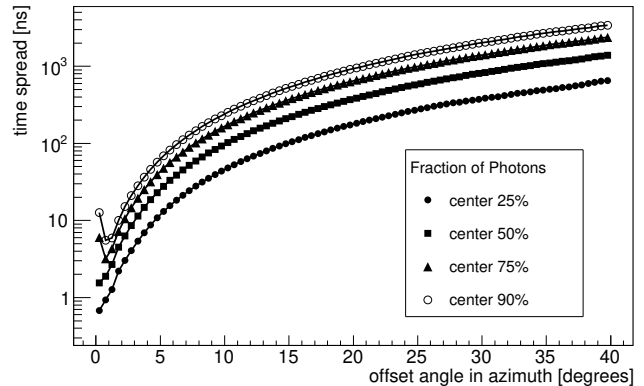


FIG. 9. Time during which Cherenkov photons arrive at the detector as a function of angle  $\alpha$ . Each curve represents a time period during which a different fraction of the Cherenkov photons arrives at the telescope. All intervals are centered at the median photon arrival time.

the photons arrive within 100 ns and if  $\alpha$  is  $40^\circ$ , the same fraction of photons arrives within  $\sim 1\text{ }\mu\text{s}$ .

## VI. FLUORESCENCE LIGHT DENSITY

Calculating the intensity of the fluorescence emission at the telescope is much simpler than for the Cherenkov emission because the emission is isotropic and concentrated to within a 130 nm wide wavelength band.

The absolute intensity of the 337 nm fluorescence line was measured by the AIRFLY Collaboration [77]. We use their measurements in our calculations but neglect variations of the intensity due to changing air pressure and temperature, and we use an average value of 6,000 photons per GeV shower energy. The same team also measured the relative intensities of the fluorescence lines between 292 nm and 428 nm [76]. We multiplied the relative intensity of each line with the PDE of the S14520-6050CN SiPM and then scaled them to the absolute intensity of the 337 nm line and arrive at an integral photoelectron intensity of 5,960 photoelectrons per GeV shower energy. The emission is, furthermore, attenuated in our calculations with an attenuation length of 9.5 km, which is the attenuation length from the VERITAS atmospheric absorption model at these wavelengths.

## VII. TRIGGER THRESHOLD

The detectability of an air shower depends not only on the amount of light that reaches the telescope but also on the minimum amount of light needed to trigger the readout electronics of the telescope, which we derive in this section. In imaging systems, a trigger decision is commonly derived by constantly monitoring the signal amplitudes of all pixels in the camera. If the signal am-



plitude of one pixel goes above a predetermined threshold that pixel is said to be triggered. But the command to read out the camera is only sent if a certain topology appears among the triggered pixels. In our study that topology consists of two pixels that trigger within a 10 ns window and are located next to each other in the camera.

In the absence of air showers, the signal of a pixel is due to electronic noise and detected background photons. SiPMs are single-photon detectors with high intrinsic gain, and the signals of individual photons, i.e. photoelectrons, are clearly identifiable in a properly designed signal chain. The trigger threshold of a pixel is thus not determined by the electronic noise but by the intensity of the photon background. This so-called night-sky background (NSB) is due to zodiacal light, airglow, star light, and artificial sources (see e.g. [91]). Due to the randomness of the photon arrival times, it can happen that the signals of photons pile up to a signal that triggers the telescope readout. The rate by which that happens depends on the intensity of the NSB, the pixel trigger threshold, the shape of the photoelectron signals, and the coincidence window. For this study, the pixel trigger threshold is set such that the expected telescope trigger rate due to NSB fluctuations is 1 Hz.

We measured the NSB with the S14520-6050CN at the Whipple Observatory in Arizona at an altitude of about 1 km above the surrounding area. Pointing the SiPM at the zenith during a clear and moonless night, we detected an NSB rate of  $3.7 \times 10^6$  photoelectrons/s/mm<sup>2</sup>/sr when the SiPM is biased at the same voltage we used for the PDE measurement shown in Fig. 6. It is expected that the NSB rate increases by a factor of 4 when the sensor is pointed at a zenith angle of 80° and that it drops again sharply for larger zenith angles because of increased scattering and attenuation in the atmosphere [91]. It is furthermore expected that, when pointing below the horizon, the detected NSB rate should be close to the rate detected when pointing at the zenith. Instead, we measured a 40 times higher NSB rate when pointing at the horizon, which was into the direction of Tucson, a city with a population of 500,000 that is 50 km away. The measurement at the horizon is thus not representative for a dark site, and we instead use the measurement at the zenith to derive pixel trigger thresholds for our acceptance and sensitivity calculations.

In order to determine the pixel trigger threshold, which results in a telescope trigger rate of 1 Hz, we first calculate the expected NSB rate  $R_D$  in a camera pixel. For this we assume a telescope with the wide field-of-view optics developed for MACHETE [92]. A MACHETE optics with a 1 m<sup>2</sup> effective mirror area and a camera with an angular resolution of 0.3° results in pixels with an area of 36 mm<sup>2</sup> and an angular acceptance of 0.842 sr. Multiplying the measured NSB rate with these values yields an  $R_D = 10^8$  counts/s per square meter effective mirror area. The dark count rate scales proportional to the area of the telescope mirror.

The rate of  $n$  photoelectrons piling up depends on  $R_D$

and the photoelectron signal shape. Here we adopt an effective signal width of  $\Delta t = 10$  ns, which is readily achievable, and assume that all photons detected within 10 ns line up perfectly. The rate  $R_n$  of  $n$  photoelectron signals piling up is then calculated as

$$R_n = R_D \left[ 1 - \sum_{i=0}^{n-1} \frac{\mu^i e^{-\mu}}{i!} \right] \quad (11)$$

where  $\mu = R_D \Delta t$  is the average number of NSB signals in  $\Delta t$ .

Finally, we calculate the telescope trigger rate for a given  $R_n$  by assuming a camera with a field of view of  $5^\circ \times 60^\circ$ , i.e. 3,333 pixels, and the aforementioned two next neighbor coincidence logic with a 10 ns coincidence window.  $R_n$  is then increased until the telescope trigger rate drops down to 1 Hz. For telescopes with effective mirror sizes of 1 m<sup>2</sup>, 5 m<sup>2</sup>, 10 m<sup>2</sup>, and 100 m<sup>2</sup> the thus derived pixel trigger thresholds are 10 pe, 22 pe, 24 pe, and 155 pe, respectively.

In the acceptance calculation we mimic a twofold coincidence trigger by requiring that the total number of detected Cherenkov photons is at least twice the single pixel threshold value. The acceptance does not depend strongly on the trigger threshold because the Cherenkov photoelectron density drops exponentially with  $\alpha$  and the distance from the telescope, which we have shown in previous sections. The biggest caveat of our simplified trigger is that it does not account for the arrival-time distribution of the Cherenkov photons, which is a few nanoseconds for small  $\alpha$  angles but can reach several hundred nanoseconds for large  $\alpha$  angles (see Fig. 9).

## VIII. ACCEPTANCE STUDIES

In this section we combine our previous findings and calculate the integral acceptance for  $10^{8.5}$  GeV to  $10^{9.5}$  GeV tau neutrinos as a function of distance from the telescope. We assume that the neutrino flux follows a power law with index  $-2$  and correspondingly weight the acceptance when integrating over neutrino energy. We do separate acceptance calculations for events detected via fluorescence emission and for those detected via Cherenkov emission.

Our baseline telescope is located 2 km above ground, has a  $5^\circ$  vertical field of view of which  $2^\circ$  point above the horizon and  $3^\circ$  point below the horizon, and has a 10 m<sup>2</sup> effective mirror area anywhere in the telescope field of view. The minimum required image length in the reconstruction is  $0.3^\circ$ . We study how changing each of these characteristics impacts the acceptance and, in doing so, show that our baseline is close to the telescope configuration, which yields the best possible sensitivity.

We start by discussing the impact of the minimum required image length in the event reconstruction. Figure 10 shows the acceptance as a function of distance between the telescope and the point where the tau emerges from

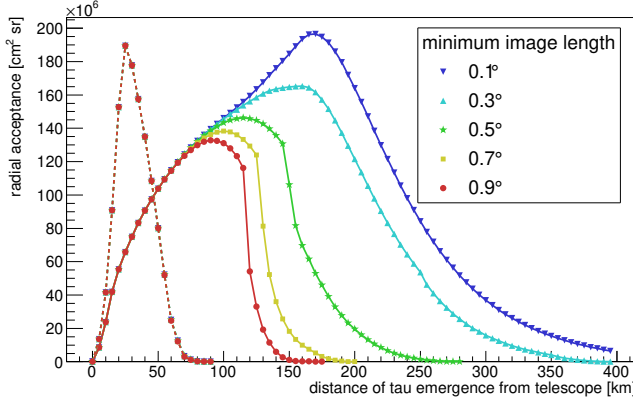


FIG. 10. Radial acceptance for different required minimum image lengths in the analysis. The dashed curves on the left give the acceptance of fluorescence detected events. The solid curves on the right give the acceptance of Cherenkov detected events.

the plane defined by  $l$  and the horizon (see Fig. 4). The acceptance is calculated in 5 km wide annuli centered at the position of the telescope. Summing the acceptance of all bins yields the total acceptance for tau neutrinos with energies from  $10^{8.5}$  GeV to  $10^{9.5}$  GeV. The dashed curves on the left give the acceptance due to fluorescence detected events while the solid curves on the right give the acceptance due to Cherenkov detected events.

As can be expected, the fluorescence emission is only detected up to a few tens of kilometers from the telescope. Furthermore, the acceptance does not depend on the minimum required image length because the showers develop so close that the length is always above the required minimum. The situation is different for Cherenkov detected events where the acceptance drops sharply above 100 km if the required image length is  $> 0.9^\circ$  but increases with a smaller required image length.

Another observation is that fluorescence detected events dominate the acceptance at small distances. This is because fluorescence detected events can be imaged from all directions, i.e. also from the back, whereas Cherenkov detected events can only be detected in a small range of  $\alpha$ . Overall, the acceptance of fluorescence detected events is about 15% of the acceptance of Cherenkov detected events if a minimum image length of  $0.1^\circ$  is required. The fraction increases to about 50% for a minimum required image length of  $0.9^\circ$ .

Figure 11 shows the acceptance for six camera fields of view above the horizon. The field of view below the horizon is not limited in these calculations. While the acceptance due to fluorescence detected events shows little dependence on the field of view above the horizon, it shows a strong dependence for Cherenkov detected events. That is because taus that emerge far away from the detector decay and produce an air shower in the camera field of view that is above the horizon. The acceptance, however, does not increase significantly if the field

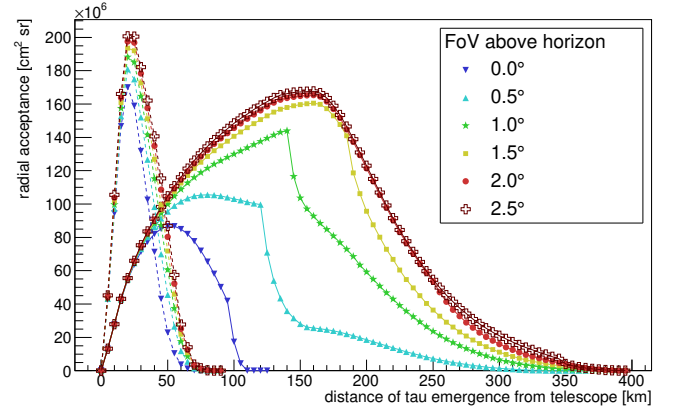


FIG. 11. Radial acceptance for different vertical fields of view of the telescope camera above the horizon. The camera field of view below the horizon is not limited. The dashed curves on the left give the acceptance of fluorescence detected events. The solid curves on the right give the acceptance of Cherenkov detected events.

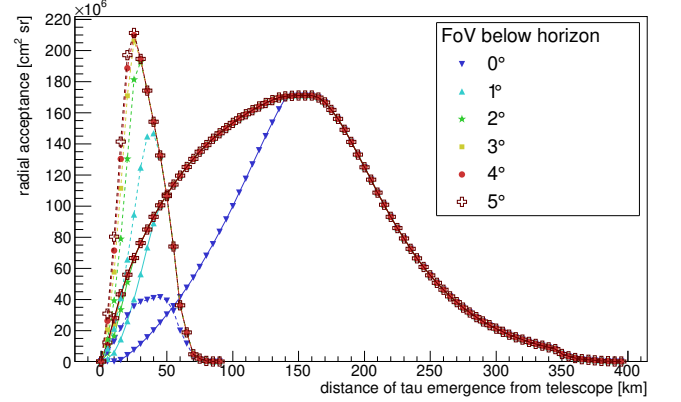


FIG. 12. Radial acceptance for different vertical fields of view of the telescope camera below the horizon. The camera field of view above the horizon is fixed at  $10^\circ$ . The dashed curves on the left give the acceptance of fluorescence detected events. The solid curves on the right give the acceptance of Cherenkov detected events.

of view above the horizon is increased beyond  $2^\circ$ . This feature can be used to define the field of view above  $2^\circ$  as a veto and thus reject potential background events due to cosmic rays.

The dependence of the acceptance on the camera field of view below the horizon shows Fig. 12. Here we fix the field of view above the horizon to  $10^\circ$ . As can be expected, the acceptance increases with an increasing field of view for events that take place within 150 km around the telescope, which is the distance to the horizon. Increasing the field of view below the horizon beyond  $1^\circ$  does not impact the acceptance of Cherenkov detected events as much as it does fluorescence detected events. The majority of fluorescence events is detected if the field of view extends to  $2^\circ$  below the horizon.

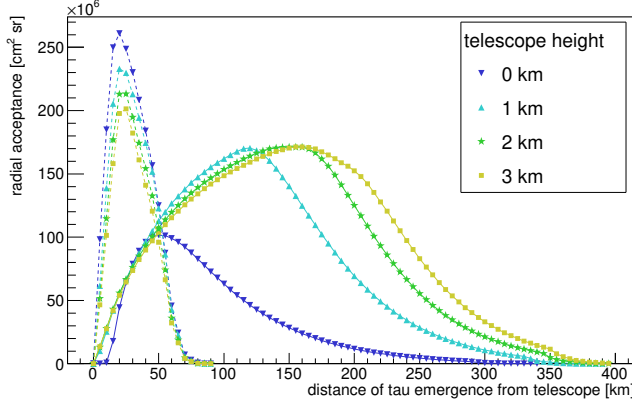


FIG. 13. Radial acceptance for different locations of the telescope above ground. The dashed curves on the left give the acceptance of fluorescence detected events. The solid curves on the right give the acceptance of Cherenkov detected events.

Figure 13 shows the acceptance for four telescope locations above ground. In order to not influence the calculation by a specific choice of the camera field of view, we did not place a limit on the field of view below the horizon and fixed the field of view above the horizon to  $10^\circ$ . While the acceptance of fluorescence detected events shows a slight decrease with an increasing telescope height above ground, the acceptance of Cherenkov detected events, which develop farther away from the telescope, clearly benefits from a telescope location that is 1 km or more above ground. That is because Cherenkov light is less attenuated at higher altitudes. For a location on the ground, the acceptance of fluorescence detected events is about the same as it is for Cherenkov detected events. When the telescope is placed 3 km above the ground, about 15% of the total acceptance is due to fluorescence detected events.

Figure 14 shows the acceptance for four different effective mirror areas. A significant increase in acceptance is seen at all distances and for both types of events as the mirror area increases from  $1 \text{ m}^2$  to  $10 \text{ m}^2$ . Increasing the mirror area by a factor of 10 from  $10 \text{ m}^2$  to  $100 \text{ m}^2$ , however, increases the acceptance by only an additional 13%.

We conclude our acceptance study with a calculation of the acceptance as a function of energy for the baseline configuration from  $10^7 \text{ GeV}$  to  $10^{11} \text{ GeV}$ . The calculation shown in Fig. 15 is done without integrating over neutrino energy; i.e. it shows the acceptance as defined by Eq. (1). For that same calculation, we show in Fig. 16 the  $\alpha$  distribution of events that trigger the readout. A total of 50% of all detected events have  $\alpha < 7^\circ$ , and 90% of all events have  $\alpha < 20^\circ$ . The remaining 10% of the events detected at larger angles are fluorescence events.

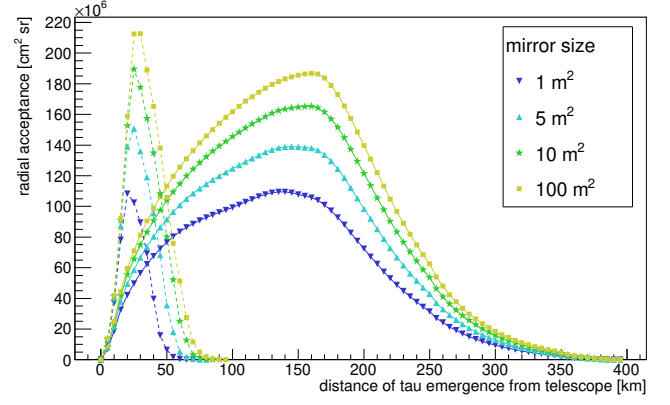


FIG. 14. Radial acceptance for different effective mirror sizes. The dashed curves on the left give the acceptance of fluorescence detected events. The solid curves on the right give the acceptance of Cherenkov detected events.

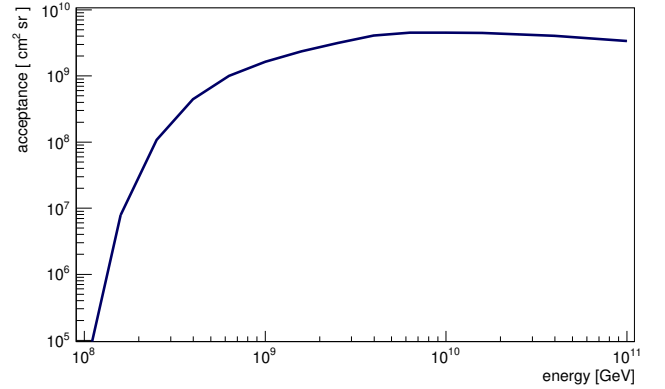


FIG. 15. Acceptance of the baseline configuration.

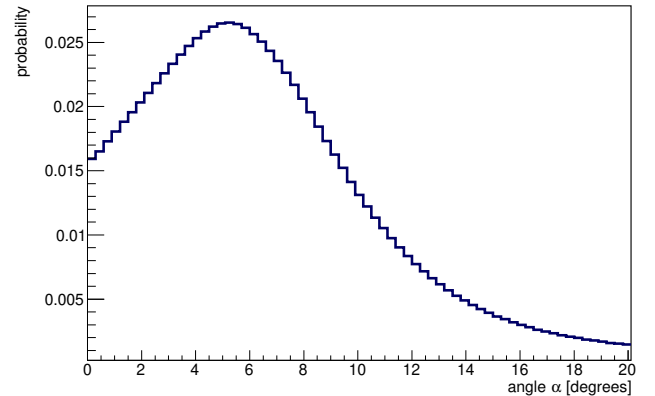


FIG. 16. The  $\alpha$  distribution of tau neutrinos with energies between  $10^7 \text{ GeV}$  and  $10^{11} \text{ GeV}$  that are detected with the baseline configuration.

## IX. SENSITIVITY

In this section we study how the sensitivity for  $10^7$  GeV to  $10^{10}$  GeV tau neutrinos is affected by different telescope parameters. For the baseline design we chose the same telescope configuration as in the previous section, and we study the impact of one parameter at a time.

The sensitivity at a given energy is calculated by integrating the acceptance over one decade of neutrino energies and centering the decade at that energy on a logarithmic scale. For the flux of the neutrinos we again assume a power law with spectral index  $-2$ . We, furthermore, require one tau-neutrino detection in three years of observation. The sensitivity is quoted for an all-flavor neutrino flux, which assumes equal mixing into all three flavors by the time the neutrinos arrive at Earth.

For the duty cycle of the observation we assume 20%, which is slightly more than the typical duty cycle of a Cherenkov telescope (14% or 1,200 hours of observations). The slightly larger duty cycle is justified because observations of tau neutrinos can also be carried out when clouds are present at high altitudes. The actual duty cycle might in fact be larger because we assume that only half of the time that is typically lost in Cherenkov telescope observations due to bad weather can still be used for neutrino observations. Tau-neutrino observations can also be carried out at brighter moonlight than gamma-ray observations, which further increases the duty cycle.

The results of the different sensitivity calculations are shown in Figs. 17–22. The solid line in each figure depicts the sensitivity of the baseline configuration.

All sensitivity curves have in common that the best sensitivity is assumed between  $2 \times 10^8$  GeV and  $4 \times 10^8$  GeV. The worsening of the sensitivity at high energies is explained with the increasing tau decay length. As a result of the increasing decay length, a decreasing fraction of high-energy taus decay and develop a full shower within the field of view of the telescope. In our calculations we neglect that some events could be viewed from the back if the tau passes across the telescope and decays within the field of view of the telescope opposite from where it originated.

The worsening of the sensitivity at lower energies is mostly due to a decrease in the emergence probability and a reduced light intensity of the air shower if the tau emerges and produces a shower.

Figure 17 shows the sensitivity for different required minimum image lengths in the reconstruction. The sensitivity improves if smaller images can be reconstructed because showers developing farther away from the telescope are accepted in the reconstruction. The sensitivity in the core energy region improves by a factor of 2 if the smallest reconstructable image length changes from  $0.9^\circ$  to  $0.1^\circ$ .

Figure 18 shows the sensitivity for different telescope locations above the ground. In order to not be affected by the choice of field of view, the upper edge of the field

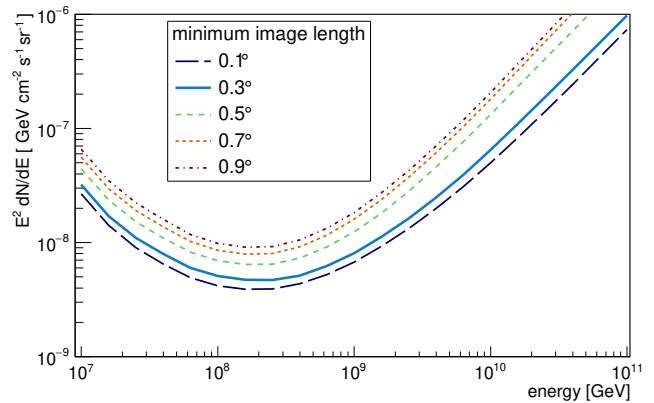


FIG. 17. Sensitivity integrated over one decade of energy for different minimal shower image lengths required in the event reconstruction.

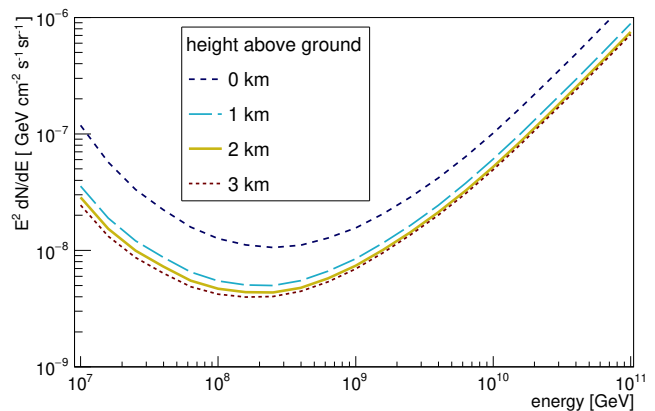


FIG. 18. Sensitivity integrated over one decade of energy for four locations of the telescope above ground.

of view is set to  $10^\circ$  above the horizon and the lower edge to  $90^\circ$  below the horizon. The most dramatic sensitivity improvements occur when the telescope is moved from the ground to a height of 1 km, which reflects the increase in acceptance to distant showers due to reduced atmospheric absorption (Fig. 13). Increasing the height above ground by an additional 2 km to 3 km improves the sensitivity by another 20%. The conclusion to draw is that the instrument is best located at an altitude between 1 km and 3 km above ground.

Figure 19 shows the sensitivity for different effective mirror sizes. Unlike in the previous two cases where about the same relative change in sensitivity is observed at all energies, an increased mirror has a bigger impact at lower energies than at higher energies. That is because dimmer showers become detectable at lower energies while the majority of the showers at higher energies are already detectable with a smaller mirror. Increasing the light collection area thus improves the sensitivity at all energies but shifts the energy where the best sensitivity is obtained toward smaller energies.

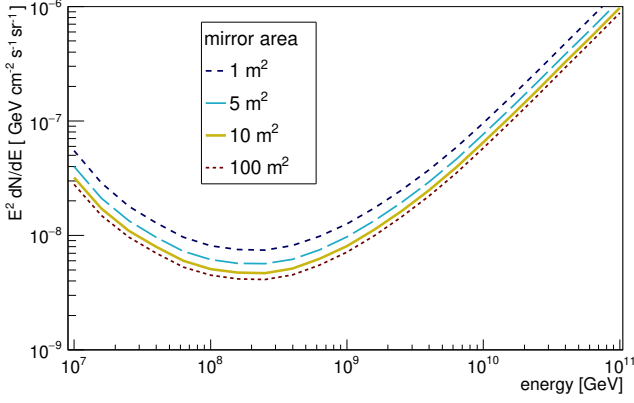


FIG. 19. Sensitivity integrated over one decade of energy for four effective mirror sizes.

An interesting observation is that the sensitivity improves by a factor of 1.6 when the mirror area increases from  $1\text{ m}^2$  to  $10\text{ m}^2$  but only by a factor of 1.2 when the mirror increases another factor of 10 from  $10\text{ m}^2$  to  $100\text{ m}^2$ . We interpret this as evidence that neutrinos, which produce an emerging tau and a subsequent particle shower are already detected with almost 100% efficiency with a  $10\text{ m}^2$  mirror surface. What we do not take into account here is that a large mirror captures fainter events and more details of shower images, which can potentially be reconstructed with a finer pixelated camera and thus could increase the sensitivity of a  $100\text{ m}^2$  class instrument beyond what our study indicates.

How the field of view of the camera above and below the horizon affects the sensitivity is shown in Figs. 20 and 21, respectively. In Fig. 20 the field of view below the horizon is fixed to  $89^\circ$ , the maximum possible value, and the field of view above the horizon is varied between  $0^\circ$  and  $10^\circ$ . At energies below  $10^8\text{ GeV}$ , the sensitivity reaches its best value already for a field of view above the horizon of  $1^\circ$ . At higher energies the sensitivity improves significantly up to a  $2^\circ$  field of view above the horizon and continues to improve by only about 20% with a further increase to  $10^\circ$ .

In Fig. 21, the field of view above the horizon is fixed at  $10^\circ$  and varied between  $0^\circ$  and  $89^\circ$  below the horizon. Increasing the field of view below the horizon to  $3^\circ$  improves the sensitivity almost to the best possible sensitivity, which is achieved if the field of view below the horizon is  $89^\circ$ . The effect of changing the field of view below the horizon is less pronounced at higher energies, which is to be expected because the majority of detectable high-energy showers originate at large distances from the telescope and develop a shower above the horizon. In other words the location of a recorded image in the camera contains information about the energy of the tau neutrino.

Combining the results from varying the field of view above and below the horizon we conclude that a camera with a vertical field of view of  $5^\circ$  and a telescope pointing

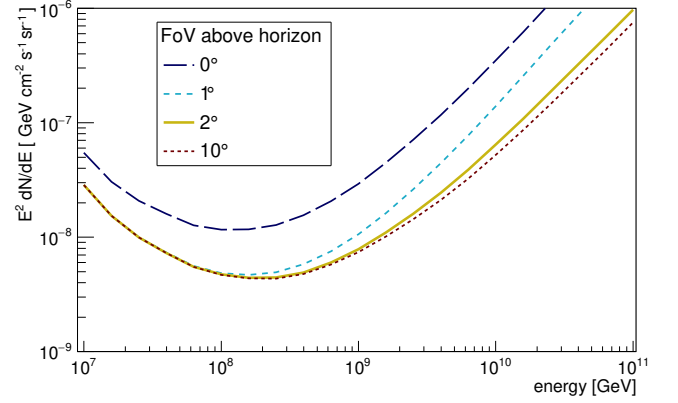


FIG. 20. Sensitivity integrated over one decade of energy for four fields of views above the horizon. The field of view below the horizon is maximal.

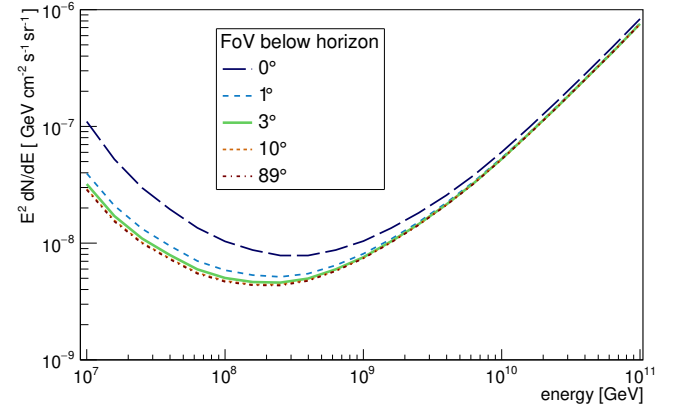


FIG. 21. Sensitivity integrated over one decade of energy for five fields of views below the horizon. The field of view above the horizon is fixed at  $10^\circ$ .

at the horizon allows one to image most events if the telescope is located 2 km above ground. This leaves  $0.5^\circ$  at the top of the field of view, which can be used as a veto. Images that are partially located in the veto region are likely due to downward going showers, meteorites, or lightning and can thus be rejected without affecting the acceptance of neutrinos.

The last effect we studied is the impact of different night-sky background levels on the sensitivity. Figure 22 shows the sensitivity of the baseline configuration for the nominal NSB intensity of  $3.7 \times 10^6$  photoelectrons/s/mm<sup>2</sup>/sr as well as for 2 and for 10 times the nominal value. The pixel trigger thresholds in increasing order of the NSB levels are 24 pe, 41 pe, and 155 pe and in each case result in a telescope trigger rate of 1 Hz due to NSB fluctuations. The sensitivity worsens with increasing NSB by about the same factor at all energies. For 2 times the NSB, the sensitivity worsens by 15%, and for 10 times the nominal NSB the sensitivity worsens by 85%. Because of the higher trigger threshold, events farther away from the telescope and those viewed



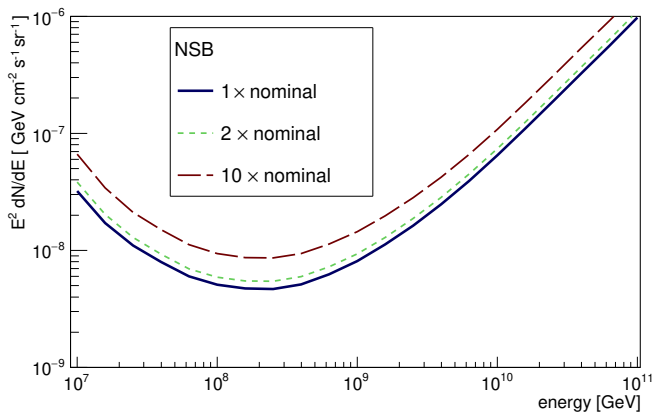


FIG. 22. Sensitivity integrated over one decade of energy for three levels of night-sky background in multiples of a nominal night-sky background of  $3.7 \times 10^6$  photoelectrons/s/mm<sup>2</sup>/sr.

at larger angles  $\alpha$  do not trigger the readout anymore. But because the Cherenkov intensity changes exponentially with distance and  $\alpha$ , the effect of a higher trigger threshold on the sensitivity is only logarithmic.

## X. TRINITY DESIGN CONSIDERATIONS

We now discuss how the above results translate into design requirements for an actual instrument, which we call *Trinity*. The basis of our study is an imaging detector with a 360° azimuthal field of view and a location on top of a mountain.

The required angular resolution of the optics across the field of view is quite modest and can be a few tenths of a degree as long as it resolves shower images above the minimum image length. Several optics concepts exist, which satisfy that requirement. A Schmidt optics, as it is used in the fluorescence detectors of TA and AUGER, is an obvious good choice [70, 71, 93]. Another option, which yields a larger azimuthal field of view with a single optical system and thus only requires six stations, is the 60° × 5° MACHETE optics [92]. Based on Fig. 19, the sensitivity approaches its optimum for an effective mirror area of 10 m<sup>2</sup>, which translates into a 4.1 m × 7.9 m mirror area of one MACHETE station.

The camera in the focal plane of the optics records the shower image. It consists of the photon detectors and the readout electronics. As already discussed, SiPMs have a spectral response, which is a good match to the Cherenkov spectrum after atmospheric absorption at the telescope. For an angular resolution of 0.3° one MACHETE camera [92] would have 3,333 pixels, each with a size of 19 mm × 19 mm. A pixel would consist of a nonimaging light concentrator coupled to a 9 mm × 9 mm SiPM.

The spread in the photon arrival times is a main driver defining the minimum sampling speed for the digitization of the SiPM signals. In Cherenkov telescopes, the

shower is typically imaged under a small angle  $\alpha < 2^\circ$ . For such small angles, the arrival-time distribution is on the order of nanoseconds and sampling speeds up into the gigasamples per second territory help to keep the contamination of the Cherenkov signal from background photons at a minimum. The fast sampling also helps in the reconstruction of events [94]. Fluorescence detectors, on the other hand, require sampling speeds of only tens of megasamples per second to capture a signal, which is spread out over several microseconds [95]. For an imaging system dedicated to the detection of tau neutrinos, a sampling speed of about 100 megasamples per second should be sufficient because the most probable value for  $\alpha$  is  $\sim 5^\circ$  (see Fig. 16) and the Cherenkov photons for that viewing angle arrive within 10 ns ··· 100 ns (see Fig. 9).

A preferred solution for the readout would be the concept used in AUGER or TA. There, the signals are continuously digitized, and the trigger decision and signal processing are accomplished digitally [70, 95, 96]. An alternative readout concept would use a switch-capacitor array that samples the signals with 100 megasamples per second. The AGET system developed for time-projection chambers could be a viable option [97].

## XI. DISCUSSION

The observation of ultrahigh-energy neutrinos has the potential to offer some unique insight into long-standing questions in astrophysics and neutrino physics. It is, therefore, not surprising that a number of experiments are proposed to explore the UHE neutrino band. In this paper we took a closer look at the possibility of detecting earth-skimming tau neutrinos with *Trinity*, an imaging system located on top of a mountain.

We find that the energy dependence of *Trinity*'s sensitivity is mostly driven by the interaction cross section of tau neutrinos and the tau decay length, with the best sensitivity being reached at  $2 \times 10^8$  GeV. Among the different telescope configurations tested, one that achieves a good compromise between performance and cost has an effective mirror area of 10 m<sup>2</sup> and is located 2 km above the ground. If the angular resolution of the camera and the optics of such a system is good enough to allow the reconstruction of shower images as small as 0.3°, a sensitivity of  $5 \times 10^{-9}$  GeV cm<sup>-2</sup> s<sup>-1</sup> sr<sup>-1</sup> per decade energy is achievable.

A comparison of *Trinity*'s sensitivity with that of GRAND [18], POEMMA [98], ARIANNA [99], ARA-37 [34], and NTA [55] is shown in Fig. 23. Also shown are predictions of the cosmogenic neutrino flux [100], measurements of the astrophysical neutrino flux with IceCube [101], and the most recent limits from IceCube [32], AUGER [49], and ANITA [29]. At energies where it has the most sensitivity, *Trinity* delivers a sensitivity that falls in between the sensitivity of proposed in-ice radio detectors and GRAND. The sensitivity is sufficient to



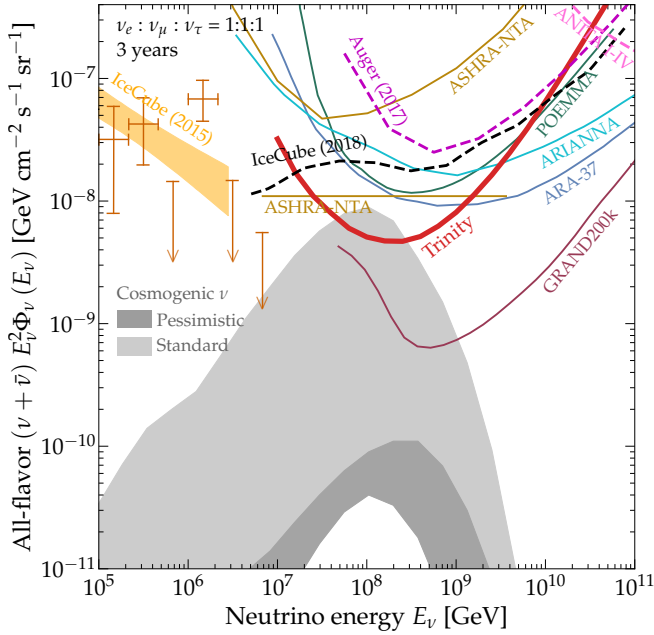


FIG. 23. Sensitivity of *Trinity* and other experiments, neutrino flux predictions, and existing flux constraints. Figure adapted from [18].

probe an extension of the IceCube detected astrophysical neutrino flux and predictions of the cosmogenic neutrino flux.

*Trinity* is complementary to in-ice radio detectors, which are sensitive to all neutrino flavors. Comparing fluxes measured with both techniques allows one to do neutrino physics at the highest energies. The very different detection techniques would also allow one to do systematic cross-checks. These cross-checks could even take place at the event level in case *Trinity* and an earth-skimming radio detector like GRAND would be deployed at the same site.

Given the expected moderate costs of *Trinity*, it is feasible to scale the system by deploying several *Trinity* sized detector stations in both hemispheres at different locations. The combined sensitivity to a diffuse neutrino flux of such a distributed system scales proportional to the number of detector stations. Furthermore, complementary parts of the sky would be observed, thus providing a better coverage in searches for astrophysical neutrino sources. It is also possible to build *Trinity* not on one site with a 360° azimuthal field of view but to deploy the six detector stations on different sites, each monitoring a different field of view and thus gaining the same sensitivity.

Because the neutrino interaction cross section and the tau decay length are dominant factors determining the sensitivity, we are open to the idea that other topographies than the one studied here could yield a higher sensitivity. In particular, a mountain range with the right height and width, as well as the right distance to the

telescope would increase the solid angle acceptance as is evidenced in [102].

For NTA it is proposed to observe taus appearing from a volcano on Mauna Loa [55]. Despite the very different topography, the integral sensitivity predicted for NTA is comparable to *Trinity*'s sensitivity (see Fig. 23), which is further evidence that other topographies are preferable to the one we studied here. An NTA-like topography has additional operational advantages. Air showers, for example, develop much closer to the telescope and the angular size of an image is, therefore, larger, which allows for a coarser angular resolution of the camera, i.e. fewer read-out channels and thus a reduction in costs. The closer proximity to the shower also increases the light intensity, thus allowing for smaller mirrors. Another advantage is reduced atmospheric absorption and an easier monitoring of the air mass, which reduces systematic uncertainties in the energy reconstruction.

The biggest uncertainty in our sensitivity calculations comes from the simplified trigger simulation and the assumption that the measurement is background free. For the trigger, we did not investigate how much the spread in arrival times for larger angles  $\alpha$  affects the trigger efficiency or what the impact of different trigger strategies is on the sensitivity. A perhaps more efficient, but also more complicated, trigger strategy than the one we studied would take the time gradient across the shower image into account.

The assumption of being background free implies that only images of tau initiated air showers survive the event reconstruction and other events triggering the readout are rejected in the analysis. Potential background events are due to fluctuations in the NSB, cosmic-ray events, and isolated muons. Background events due to fluctuations in the NSB are reliably suppressed by the standard principal component analysis of air-shower images. Cosmic-ray air showers at large zenith angles develop at much larger distances. Their light is, therefore, subject to more absorption and scattering. Cosmic-ray showers, furthermore, start above the horizon, whereas tau showers start below the horizon, which can be distinguished based on the time and spatial characteristics of the recorded shower images, and their location in the camera. Isolated muons could be another source of background events, which becomes important for larger mirror surfaces than considered here. Muon events are easily suppressed by operating two detector stations separated by more than 100 m. They can also be rejected based on the much narrower photon arrival-time distribution of only a few nanoseconds compared to several tens to hundreds of nanoseconds for a tau initiated shower. How well these background events can be suppressed remains to be seen and is best assessed with observations.

We conclude that the imaging of air showers is a viable technique to detect tau neutrinos. Combined with recent advances in the SiPM technology and affordable readout options with sampling speeds in the 100 MS/s range, a *Trinity*-like detector is a cost effective and robust way to

detect tau neutrinos with competitive sensitivity.

## ACKNOWLEDGMENTS

This project was started by a discussion with Albrecht Karle at VHEPA in 2016. I am grateful for the many discussions I had with him and a number of other colleagues over the past three years. Mary Hall Reno provided insight into the calculations of the tau emergence probabilities. Juan Cortina provided insight

about the expected optical resolution of a scaled MACHETE. Abelardo Moralejo and Michael Unger gave valuable feedback about the shower and Cherenkov light parametrization and the detector configuration. Mauricio Bustamante was so kind to provide me with Fig. 23. Dieter Heck's relentless support has proved vital in my effort to set up the CORSIKA simulations and to understand the simulation results.

## REFERENCES

- 
- [1] M. G. Aartsen *et al.* (IceCube Collaboration), *Science* **342**, 1242856 (2013), arXiv:1311.5238.
  - [2] M. G. Aartsen *et al.* (IceCube, Fermi-LAT, MAGIC, AGILE, ASAS-SN, HAWC, H.E.S.S., INTEGRAL, Kanata, Kiso, Kapteyn, Liverpool Telescope, Subaru, Swift/NuSTAR, VERITAS, and VLA/17B-403 Collaborations), *Science* **361**, eaat1378 (2018), arXiv:1807.08816.
  - [3] M. G. Aartsen *et al.* (IceCube Collaboration), *Science* (New York, N.Y.) **361**, 147 (2018).
  - [4] W. Waxman and J. Bahcall, *Phys. Rev. Lett.* **78**, 2292 (1997), arXiv:astro-ph/9701231 [astro-ph].
  - [5] P. Mészáros and E. Waxman, *Phys. Rev. Lett.* **87** (2001), 10.1103/PhysRevLett.87.171102, arXiv:astro-ph/0103275 [astro-ph].
  - [6] A. Loeb and E. Waxman, *J. Cosmol. Astropart. Phys.* (2006), 10.1088/1475-7516/2006/05/003, arXiv:astro-ph/0601695 [astro-ph].
  - [7] N. Senno, K. Murase, and P. Mészáros, *Phys. Rev. D* **93** (2016), 10.1103/PhysRevD.93.083003, arXiv:1512.08513.
  - [8] M. Ahlers and F. Halzen, *Progress in Particle and Nuclear Physics* **102**, 73 (2018).
  - [9] K. Kotera, D. Allard, and A. V. Olinto, *J. Cosmol. Astropart. Phys.* **2010**, 013 (2010), arXiv:1009.1382.
  - [10] K. H. Kampert and M. Unger, *Astropart. Phys.* **35**, 660 (2012), arXiv:1201.0018.
  - [11] A. Aab *et al.* (Pierre Auger Collaboration), *Phys. Lett. B* **762**, 288 (2016), arXiv:1609.08567.
  - [12] R. U. Abbasi *et al.* (Telescope Array Collaboration), *Astropart. Phys.*, Volume 64, p. 49-62. **64**, 49 (2015), arXiv:1408.1726.
  - [13] A. Yushkov, in *ISVHECRI 2016*, Vol. 145, edited by B. Pattison (EPJ Web of Conferences, Moscow, 2017) p. 05002.
  - [14] A. Aab *et al.* (Pierre Auger Collaboration), *J. Cosmol. Astropart. Phys.* **2017**, 038 (2017).
  - [15] A. Aab *et al.* (Pierre Auger Collaboration), *Phys. Rev. D* **96**, 122003 (2017).
  - [16] A. van Vliet, R. Alves Batista, and J. Hörandel, in *ICRC2017*, Vol. 301 (Sissa Medialab, Busan, 2017) p. 562.
  - [17] K. Möller, P. B. Denton, and I. Tamborra, (2018), arXiv:1809.04866.
  - [18] J. Alvarez-Muniz *et al.* (GRAND Collaboration), (2018), arXiv:1810.09994.
  - [19] P. W. Gorham *et al.* (ANITA Collaboration), *Phys. Rev. Lett.* **121**, 161102 (2018), arXiv:1803.05088.
  - [20] S. R. Klein and A. Connolly, (2013), arXiv:1304.4891.
  - [21] D. B. Fox, S. Sigurdsson, S. Shandera, P. Mészáros, K. Murase, M. Mostafá, and S. Coutu, (2018), arXiv:1809.09615.
  - [22] V. A. Ryabov, *Physics-Uspekhi* **49**, 905 (2006).
  - [23] B. T. Cleveland, T. Daily, R. Davis, Jr., J. R. Distel, K. Lande, C. K. Lee, P. S. Wildenhain, and J. Ullman, *The Astrophysical Journal* **496**, 505 (1998).
  - [24] Y. Fukuda *et al.* (Super-Kamiokande Collaboration), *Phys. Rev. Lett.* **81**, 1562 (1998), arXiv:hep-ex/9807003 [hep-ex].
  - [25] Q. R. Ahmad *et al.* (SNO Collaboration), *Phys. Rev. Lett.* **87**, 071301 (2001).
  - [26] Q. R. Ahmad *et al.* (SNO Collaboration), *Phys. Rev. Lett.* **89**, 011301 (2002), arXiv:nuclex/0204008 [nucl-ex].
  - [27] M. G. Aartsen *et al.* (IceCube Collaboration), *Nature* **551**, 596 (2017), arXiv:1711.08119.
  - [28] M. Aartsen *et al.* (IceCube Collaboration), *Phys. Rev. Lett.* **120**, 071801 (2018).
  - [29] P. W. Gorham *et al.* (ANITA Collaboration), (2019), arXiv:1902.04005.
  - [30] M. Ageron *et al.* (ANTARES Collaboration), *Nuclear Instruments and Methods in Physics Research Section A: Accelerators, Spectrometers, Detectors and Associated Equipment* **656**, 11 (2011).
  - [31] S. Adrián-Martínez *et al.* (KM3NeT Collaboration), *Journal of Physics G: Nuclear and Particle Physics* **43**, 084001 (2016).
  - [32] M. Aartsen *et al.* (IceCube Collaboration), *Phys. Rev. D* **98** (2018), 10.1103/PhysRevD.98.062003.
  - [33] P. Allison *et al.* (ARA Collaboration), *Astropart. Phys.* **70**, 62 (2015), arXiv:1404.5285.
  - [34] P. Allison *et al.* (ARA Collaboration), *Phys. Rev. D* **93** (2016), 10.1103/PhysRevD.93.082003, arXiv:astro-ph.HE/1507.08991 [astro-ph.HE].
  - [35] S. W. Barwick *et al.* (ARIANNA), *Astropart. Phys.* **70**, 12 (2015), arXiv:1410.7352.
  - [36] S. Barwick *et al.* (ARIANNA), *Astropart. Phys.* **90**, 50 (2017).
  - [37] S. W. Barwick *et al.* (ANITA Collaboration), *Phys. Rev. Lett.* **96**, 171101 (2006), arXiv:astro-ph/0512265 [astro-ph].

- [38] P. Gorham *et al.* (ANITA Collaboration), Phys. Rev. Lett. **117**, 071101 (2016).
- [39] P. Gorham *et al.* (ANITA Collaboration), Phys. Rev. D **98** (2018), 10.1103/PhysRevD.98.022001.
- [40] A. L. Connolly and A. G. Vieregge, (2016), arXiv:1607.08232.
- [41] F. G. Schröder, Progress in Particle and Nuclear Physics **93**, 1 (2017).
- [42] D. Fargion, A. Aiello, and R. Conversano, (1999), arXiv:astro-ph/9906450 [astro-ph].
- [43] D. Fargion, in *HEP2001*, edited by D. Horvath, P. Levai, and A. Patkos (JHEP, Budapest, 2001) arXiv:hep-ph/0111289 [hep-ph].
- [44] D. Fargion, (2001), arXiv:astro-ph/0107094 [astro-ph].
- [45] D. Fargion, The Astrophysical Journal **570**, 909 (2002).
- [46] J. L. Feng, P. Fisher, F. Wilczek, and T. M. Yu, Phys. Rev. Lett. **88**, 161102 (2002), arXiv:hep-ph/0105067 [hep-ph].
- [47] D. Fargion, M. Grossi, M. De Santis, P. G. De Sanctis Lucentini, M. Iori, A. Sergi, and F. Moscato, Advances in Space Research **37**, 2132 (2006), arXiv:astro-ph/0501079v2 [arXiv:astro-ph].
- [48] A. Aab *et al.* (Pierre Auger Collaboration), Phys. Rev. D **91**, 092008 (2015).
- [49] A. Aab *et al.* (Pierre Auger Collaboration), (2017), arXiv:1708.06592.
- [50] F. Pedreira (Pierre Auger Collaboration), in *Neutrino 2018* (Heidelberg, 2018).
- [51] M. Gaug, C. Hsu, J. K. Becker, A. Biland, M. Mariotti, W. Rhode, and M. Teshima, in *ICRC2007*, Vol. 32 (Merida, 2007) pp. 21–21, arXiv:0709.1462.
- [52] M. L. Ahnen *et al.* (MAGIC Collaboration), Astropart. Phys. **102**, 77 (2018), arXiv:1805.02750.
- [53] O. Martineau *et al.* (GRAND Collaboration), in *ICRC2015*, Vol. 34 (The Hague, 2015).
- [54] M. Bustamante, in *VHEPA 2016* (Honolulu, 2016).
- [55] M. Sasaki and G. W.-S. Hou, (2014), arXiv:1408.6244.
- [56] G. W. S. Hou and M. Sasaki, in *VHEPA2014* (Kashiwa, Tokyo, 2015) arXiv:1409.0477.
- [57] Y. Asaoka and M. Sasaki, Astropart. Phys., Volume 41, p. 7-16. **41**, 7 (2013), arXiv:1202.5656.
- [58] A. Neronov, D. V. Semikoz, L. A. Anchordoqui, J. Adams, and A. V. Olinto, Phys. Rev. D, 15 (2017), arXiv:1606.03629.
- [59] J. H. Adams, L. A. Anchordoqui, J. A. Apple, M. E. Bertaina, M. J. Christl, F. Fenu, E. Kuznetsov, A. Neronov, A. V. Olinto, E. Parizot, T. C. Paul, G. Prevot, P. Reardon, I. Vovk, L. Wiencke, and R. M. Young, *White paper on EUSO-SPB2*, Tech. Rep. (2017) arXiv:1703.04513.
- [60] A. V. Olinto *et al.* (POEMMA Collaboration), in *ICRC2017* (Busan, Korea, 2017) arXiv:1708.07599.
- [61] P. Yeh *et al.* (NuTel Collaboration), Modern Phys. Lett. A **19**, 1117 (2004).
- [62] J. L. Liu *et al.* (CRTNT Collaboration), Journal of Physics G: Nuclear and Particle Physics **36**, 075201 (2009).
- [63] Z. Cao, M. A. Huang, P. Sokolsky, and Y. Hu, Journal of Physics G: Nuclear and Particle Physics **31**, 571 (2005).
- [64] J. Aleksić *et al.* (MAGIC Collaboration), Astropart. Phys. **72**, 76 (2016), arXiv:1409.5594.
- [65] A. Cooper-Sarkar, P. Mertsch, and S. Sarkar, Journal of High Energy Physics **2011** (2011), 10.1007/JHEP08(2011)042, arXiv:1106.3723.
- [66] S. Archambault *et al.* (VERITAS Collaboration), Astropart. Phys. **91**, 34 (2017), arXiv:1703.01307.
- [67] F. Aharonian *et al.* (H.E.S.S. Collaboration), Astronomy & Astrophysics **457**, 899 (2006), arXiv:astro-ph/0607333 [astro-ph].
- [68] J. Aleksić *et al.* (MAGIC Collaboration), Journal of High Energy Astrophysics **5-6**, 30 (2015), arXiv:1406.6892.
- [69] M. Actis *et al.* (CTA Collaboration), Experimental Astronomy **32** (2011), 10.1007/s10686-011-9247-0.
- [70] J. Abraham *et al.* (Pierre Auger Collaboration), NIM A **620**, 227 (2010).
- [71] R. Abbasi *et al.* (Telescope Array Collaboration), Astropart. Phys. **64**, 49 (2015).
- [72] S. I. Dutta, Y. Huang, and M. H. Reno, Phys. Rev. D **72**, 1 (2005), arXiv:hep-ph/0504208 [hep-ph].
- [73] J. Alvarez-Muñiz, W. R. Carvalho, K. Payet, A. Romero-Wolf, H. Schoorlemmer, and E. Zas, Phys. Rev. D **97** (2018), 10.1103/PhysRevD.97.023021, arXiv:1707.00334.
- [74] J. Alvarez-Muñiz, W. R. Carvalho, A. L. Cummings, K. Payet, A. Romero-Wolf, H. Schoorlemmer, and E. Zas, (2019), arXiv:1901.08498.
- [75] See figure 1 for a definition of  $\epsilon$ .
- [76] M. Ave *et al.* (AIRFLY), Astropart. Phys. **28**, 41 (2007), arXiv:astro-ph/0703132 [astro-ph].
- [77] M. Ave *et al.* (AIRFLY), Astropart. Phys. **42**, 90 (2013), arXiv:1210.6734 [astro-ph.IM].
- [78] M. S. Longair, *High energy astrophysics* (Cambridge University Press, 2011) p. 861.
- [79] W. Heitler, *The quantum theory of radiation* (Dover Publications, 1984) p. 430.
- [80] M. Tanabashi *et al.* (Particle Data Group), Phys. Rev. D **98** (2018), 10.1103/PhysRevD.98.030001.
- [81] D. Heck, J. Knapp, J. N. Capdevielle, G. Schatz, and T. Thouw, CORSIKA: a Monte Carlo code to simulate extensive air showers., Forschungszentrum Karlsruhe GmbH, Karlsruhe (Germany)., V + 90 p., TIB Hannover, D-30167 Hannover (Germany). **6019** (1998).
- [82] “MODTRAN<sup>®</sup>,” <http://modtran.spectral.com/> (2018).
- [83] K. Louedec and J. Colombi, Astropart. Phys. **57-58**, 6 (2014).
- [84] M. Giller and A. Śmiałkowski, Astropart. Phys. **36**, 166 (2012).
- [85] Note that unlike what is depicted, we assume a flat Earth surface for the absorption calculation.
- [86] D. Renker and E. Lorenz, Journal of Instrumentation **4**, P04004 (2009).
- [87] A. N. Otte, in *PhotoDet2015* (PoS, Moscow, 2015).
- [88] A. N. Otte, D. Garcia, T. Nguyen, and D. Purushotham, NIM A **846**, 106 (2017), arXiv:1606.05186.
- [89] A. N. Otte, T. Nguyen, and J. Stansbury, NIM A (2018), arXiv:1808.00487.
- [90] F. Nerling, J. Blümer, R. Engel, and M. Risse, Astropart. Phys. **24**, 421 (2006), arXiv:astro-ph/0506729 [astro-ph].
- [91] C. Leinert *et al.*, Astronomy and Astrophysics Supplement Series **127**, 1 (1998).
- [92] J. Cortina, R. López-Coto, and A. Moralejo, Astropart. Phys. **72**, 46 (2016), arXiv:1507.02532v1.

- [93] H. Tokuno *et al.* (Telescope Array Collaboration), NIM A **676**, 54 (2012).
- [94] E. Aliu *et al.* (MAGIC Collaboration), Astropart. Phys. **30**, 293 (2009).
- [95] H. Gemmeke, A. Grindler, H. Keim, M. Kleifges, N. Kunka, Z. Szadkowski, and D. Tcherniakhovski, IEEE Transactions on Nuclear Science **47**, 371 (2000).
- [96] Y. Tameda *et al.* (Telescope Array Collaboration), NIM A **609**, 227 (2009).
- [97] E. Pollacco, G. Grinyer, F. Abu-Nimeh, T. Ahn, S. Anvar, A. Arokiaraj, Y. Ayyad, H. Baba, M. Babo, P. Baron, *et al.*, NIM A **887**, 81 (2018).
- [98] J. F. Krizmanic, in *Ultra High Energy Cosmic Rays Conference 2018 (UHECR 2018)* (Paris, 2018).
- [99] C. R. Persichilli, *Performance and Simulation of the ARIANNA Pilot Array, with Implications for Future Ultra-high Energy Neutrino Astronomy*, Ph.D. thesis, University of California, Irvine (2018).
- [100] R. A. Batista, R. M. de Almeida, B. Lago, and K. Kotera, J. Cosmol. Astropart. Phys. **2019**, 002 (2019), arXiv:1806.10879.
- [101] M. G. Aartsen *et al.* (IceCube Collaboration), Astrophysical Journal **809** (2015), 10.1088/0004-637X/809/1/98, arXiv:1507.03991.
- [102] D. Góra, E. Bernardini, and A. Kappes, Astropart. Phys. **61**, 12 (2015).